BRAIN
ORIGINAL ARTICLE

Somatic variants of *MAP3K3* are sufficient to cause cerebral and spinal cord cavernous malformations

Jian Ren,[1,†] Yazi Huang,[2,†] Yeqing Ren,[1,†] Tianqi Tu,[1] Baoshan Qiu,[2,3] Daosheng Ai,[2,4] Zhanying Bi,[2,5] Xue Bai,[2] Fengzhi Li,[2] Jun-Liszt Li,[2,4] Xing-jun Chen,[2,4] Ziyan Feng,[2] Zongpei Guo,[2] Jianfeng Lei,[6] An Tian,[1] Ziwei Cui,[1] Volkhard Lindner,[7] Ralf H. Adams,[8] Yibo Wang,[9] Fei Zhao,[2] Jakob Körbelin,[10] Wenzhi Sun,[2,11] Yilong Wang,[3] Hongqi Zhang,[1] Tao Hong[1] and Woo-ping Ge[2,12]

[†]These authors contributed equally to this work.

Cerebral cavernous malformations (CCMs) and spinal cord cavernous malformations (SCCMs) are common vascular abnormalities of the CNS that can lead to seizure, haemorrhage and other neurological deficits. Approximately 85% of patients present with sporadic (versus congenital) CCMs. Somatic mutations in *MAP3K3* and *PIK3CA* were recently reported in patients with sporadic CCM, yet it remains unknown whether *MAP3K3* mutation is sufficient to induce CCMs. Here we analysed whole-exome sequencing data for patients with CCM and found that ∼40% of them have a single, specific *MAP3K3* mutation [c.1323C>G (p.Ile441Met)] but not any other known mutations in CCM-related genes.

We developed a mouse model of CCM with *MAP3K3*^{I441M} uniquely expressed in the endothelium of the CNS. We detected pathological phenotypes similar to those found in patients with *MAP3K3*^{I441M}. The combination of *in vivo* imaging and genetic labelling revealed that CCMs were initiated with endothelial expansion followed by disruption of the blood–brain barrier. Experiments with our *MAP3K3*^{I441M} mouse model demonstrated that CCM can be alleviated by treatment with rapamycin, the mTOR inhibitor. CCM pathogenesis has usually been attributed to acquisition of two or three distinct genetic mutations involving the genes *CCM1/2/3* and/or *PIK3CA*. However, our results demonstrate that a single genetic hit is sufficient to cause CCMs.

1 Department of Neurosurgery, Xuanwu Hospital, China International Neuroscience Institute, Capital Medical University, Beijing 100053, China
2 Chinese Institute for Brain Research, Beijing 102206, China
3 Department of Neurology, Beijing Tiantan Hospital, Capital Medical University, Beijing 100070, China
4 Academy for Advanced Interdisciplinary Studies (AAIS), Peking University, Beijing 100871, China
5 College of Life Sciences, Nankai University, Tianjin 300071, China
6 Medical Imaging laboratory of Core Facility Center, Capital Medical University, Beijing 100054, China
7 Center for Molecular Medicine, MaineHealth Institute for Research, Scarborough, ME 04074, USA
8 Department of Tissue Morphogenesis, Max-Planck-Institute for Molecular Biomedicine, and Faculty of Medicine, University of Münster, D-48149 Münster, Germany
9 State Key Laboratory of Cardiovascular Disease, Fuwai Hospital, National Center for Cardiovascular Diseases, Chinese Academy of Medical Sciences and Peking Union Medical College, Beijing 100037, China
10 Department of Oncology, Hematology and Bone Marrow Transplantation, University Medical Center Hamburg-Eppendorf, Hamburg 20246, Germany

Received July 21, 2022. Revised March 07, 2023. Accepted March 12, 2023. Advance access publication March 30, 2023

11 School of Basic Medical Sciences, Capital Medical University, Beijing 100054, China
12 Department of Neurosurgery, Xuanwu Hospital, Beijing Institute of Brain Disorders (BIBD), China International Neuroscience Institute, Capital Medical University, Beijing 100053, China

Correspondence to: Woo-ping Ge, PhD
Chinese Institute for Brain Research, Beijing(CIBR)
9 Yi-Ke Rd, Zhongguancun Life Science Park
Changping District, Beijing 102206, China
E-mail: woopingge@cibr.ac.cn

Correspondence may also be addressed to: Tao Hong, MD, PhD
Department of Neurosurgery, Xuanwu Hospital, Capital Medical University
45 Changchun St, Beijing, 100053, China
E-mail: hongtao.edu@gmail.com

Keywords: *MAP3K3*; somatic mutation; cavernous malformations; cerebral; spinal cord; endothelial cell

Introduction

Cerebral cavernous malformations (CCMs) and spinal cord cavernous malformations (SCCMs) are common vascular abnormalities of the CNS, affecting ~0.16–0.40% of the population worldwide.[1,2] The thinned, enlarged and leaky plasma membrane of endothelial cells that is characteristic of CCMs and SCCMs increases the risk of stroke, seizures and focal neurological deficits.[3] Currently, no drug is available to treat SCCMs or CCMs.[4]

The propensity to develop CCMs can be inherited. Biallelic loss-of-function (LOF) mutations in three genes, namely *KRIT1* (*CCM1*), *CCM2* and *PDCD10* (*CCM3*), have been identified as causative in familial CCMs.[5-7] Although CCM lesions were once believed to be congenital, most CCMs are sporadic and usually detected in patients between the third and fourth decades of life. The *de novo* formation of sporadic CCMs in patients has been frequently reported,[3,8] and nearly 85% of CCMs are sporadic.[9,10] Our team and others recently reported that somatic mutations in *MAP3K3* and *PIK3CA* are common in sporadic CCMs and SCCMs,[11-15] but it remains unknown whether *MAP3K3* mutations are the key driver of CCM and SCCM formation and pathogenesis in patients.

The aetiology of CCMs related to *CCM1/2/3* mutations has been attributed to a two-hit mechanism, i.e. mutations in two of the three CCM genes.[5-7,16] Recently, however, a three-hit mechanism was proposed for severe CCMs, positing that gain-of-function (GOF) somatic mutation of the oncogene *PIK3CA* in addition to LOF *CCM1/2/3* mutations increases CCM severity.[15] Surprisingly, however, neither LOF of *CCM1/2/3* nor GOF of *PIK3CA* alone is able to drive vascular cavernous malformations (CMs) in the brain of adult mice.[15,17-20] Here, we report that a high percentage (66%) of all *MAP3K3*^{I441M}-mutated CCM patients have a singular *MAP3K3*^{I441M} mutation without any other known mutations in CCM-related genes (e.g. *CCM1/2/3*, *PIK3CA*, etc.). Through establishing a mouse model of CCM in which *MAP3K3*^{I441M} is uniquely expressed in the endothelium of the CNS, we show that expression of the *MAP3K3*^{I441M} mutant alone caused CCMs and SCCMs in mice of different ages. The CCM pathological phenotypes in this mouse model were similar to what has been observed in human sporadic CCM lesions. *In vivo* time-lapse imaging of the mature brain from *MAP3K3*^{I441M} mice revealed the formation of CCMs with dilated, low-flow and leaky caverns. *MAP3K3*^{I441M} initiated CCM formation by upregulating the production of the cytoskeleton and increasing the size of individual endothelial cells. Our results also demonstrated that *MAP3K3*^{I441M} can activate the mTOR (mammalian target of rapamycin) pathway. Blocking mTOR with rapamycin slowed CCM progression.

Materials and methods

Animals

All mouse experiments were conducted in accordance with protocols approved by the Institutional Animal Care and Use Committee (IACUC) at the Chinese Institute for Brain Research, Beijing. *NG2DsRedBAC* (Cat. No. 008241) and *Ai14* transgenic mouse strains (Cat. No. 007908) were purchased from Jackson Lab. *Pdgfrb-Cre* and *Cdh5-CreER* were acquired from Volkhard Lindner and Ralf H. Adams's laboratories, respectively.

Plasmid construction, adeno-associated virus packaging and injection

MAP3K3^{I441M} cDNA fragment was cloned into the *pAAV-CAG-EGFP* vector via adding a P2A sequence between *MAP3K3* and *EGFP*, generating the plasmid *pAAV-CAG-MAP3K3*^{I441M}*-P2A-EGFP*. A *pXX2-187-NRGTEWD* (termed 'BR1') plasmid containing the adeno-associated virus (AAV) rep/cap genes with a sequence translating into a brain vascular endothelial-targeting peptide (NRGTEWD) from the laboratory of Jakob Körbelin.[21] Three plasmids, including *pAAV-CAG-MAP3K3*^{I441M}*-P2A-EGFP*, *pXX2-187-NRGTEWD* and a helper vector (pAdDeltaF6), were transfected into HEK293T cells via Lipofectamine 2000. The *AAV-BR1-MAP3K3*^{I441M}*-P2A-EGFP* capsids were harvested and purified 72 h later. Mice were injected with *AAV-BR1-MAP3K3* ^{I441M}*-P2A-EGFP* (3×10^{11} genome copies per mouse) through the superficial temporal vein.[22]

MRI evaluation

We performed MRI experiments on a Bruker 7.0 T MRI scanner (Bruker Pharmascan 70/16). A 23 mm surface coil and a 12-cm diameter self-shielded gradient system were equipped to acquire signals. The user interface was Paravision 5.1 software (Bruker BioSpin) and a Linux PC running Topspin 2.0. For mouse anaesthetization, 5% isoflurane and 95% O_2 mixture were used for induction

in a plexiglass chamber, and 2% isoflurane/98% O_2 mixture was used for maintenance in the centre of the magnetic field. Respiratory rate was closely monitored by an animal physiological guarding system. T_2-weighted imaging was performed with a rapid acquisition method with relaxation enhancement (RARE). The detailed parameters were as follows: repetition time: 3500 ms, echo time: 33 ms, RARE factor: 4, field of view: 21 × 21 mm, acquisition matrix: 256 × 256, and slice thickness: 0.5 mm. The number of lesions was quantified from T_2-weighted images.

Cranial window preparation and live imaging

Before *in vivo* imaging, a chronic cranial window was made as previously reported.[23] Briefly, mice (1–2 months old) were anaesthetized with isoflurane (5% for induction, 2% for maintenance) and fixed in a homemade stereotaxic frame. Mice were kept warm with a heating pad during the operation. Dexamethasone (100 μl, 1 mg/ml in saline) was injected intraperitoneally before surgery. A craniotomy (3 mm in diameter) was made over the somatosensory cortex (1–2 mm lateral and 1–2.5 mm posterior to bregma) with a dental drill. A sterile coverslip (3 mm in diameter) with a customized titanium ring was placed on the window and sealed with cyanoacrylate glue. Dental cement was applied to the remaining exposed skull surface. Finally, a custom-made head plate was attached to the skull with dental cement. All surgical procedures were kept sterile. Ceftiofur sodium (100 μl, 0.1 g/ml, saline) was injected intraperitoneally in the following 3 days. Mice were allowed to recover for at least 2 weeks after surgery before we performed live imaging.

Observation was usually performed 2–3 weeks after AAV injection. For live imaging of the brain vasculature, head-fixed mice were placed on a customized microscope stage. To exclude the effect of anaesthesia on cerebral blood flow, mice were imaged in a state of consciousness. Mice were trained to accustom them to the platform for at least 30 min each day for 3 days before imaging. To observe blood flow, FITC-dextran dye (2000 kDa, Sigma) at a dose of 100 μl (1% w/v, saline) was injected through the retro-orbital vein. Cerebral vasculature was observed by an upright two-photon laser scanning microscope (TPLSM, FVMPE-RS, Olympus) controlled by software (F31S-SW, Olympus) and a Mai Tai HP Ti:Sapphire laser (InSight X3™, spectra physics) with a 25 × 1.05 NA water immersion objective lens (Olympus) at a 1024 × 1024 pixel resolution, with galvanometric scanners. The optimal excitation wavelength was set as 990 nm for both FITC and Dsred. The emitted fluorescence from FITC and Dsred was detected with a non-descanned GaAsp detector (Olympus) and emission bandpass filters were BA575-645 (red) and BA495-540 (green). Z-stack images were collected at 2-μm step size in a volume of 509 × 509 × 500 μm. For the measurement of red blood cell velocity in each capillary, X-T line scanning was conducted along a 15–50 μm range for 2000 cycles.

Histological staining

Mice were perfused with PBS followed with 4% paraformaldehyde (PFA). Brain tissues were collected and paraffin-embedded sections (6 μm) were stained with haematoxylin and eosin (H&E), Prussian blue and antibodies against Ki67. Stained sections were imaged on a VS120 Virtual Slide Microscope (Olympus).

Immunostaining

Brains were collected and embedded with optimal cutting temperature compound (OCT compound) after perfusion as described. Frozen sections (40 μm) were incubated with primary antibodies against CD31 (1:100; BD Biosciences, 550274), Collagen IV (1:100; Merk-millipore, AB756P), p62 (1:200; Abcam, ab56416), Laminin (1:400; Sigma, L9393), S6 Kinase (1:200, Cell Signaling Technologies, 34475, or cleaved Caspase-3 (1:100, Cell Signaling Technologies, 9661) for 48 h at 4°C, and then stained with the related secondary antibodies conjugated with Alexa Fluor 546 (1:500; Thermo) or Alexa Fluor 647 (1:500; Thermo) as well as DAPI or Hoechst 33342 (0.5 μg/ml; Sigma) for 2 h at room temperature. Sections were mounted on glass slides. Images were acquired via Leica SP8 confocal microscope. For confocal imaging, the following wavelengths were used: 405 nm for DAPI or Hoechst 33342, 488 nm for GFP, 552 nm for tdTomato/DsRed or Alexa Fluor 546, and 638 nm for Alexa Fluor 647.

Clinical specimens of human samples

Frozen CM samples obtained from 104 patients were used for mutation analysis with whole-exome sequencing and/or droplet digital polymerase chain reaction (ddPCR). Paraffin-embedded sections from five patients with *MAP3K3*^{I441M} were used for histological staining and immunostaining. The control samples ($n = 2$ patients) were temporal lobe tissue from patients with temporal lobe epilepsy but no CCMs. One sample of a glioma was used for immunostaining for Ki67. All the patients included in this study underwent surgical resection at Xuanwu Hospital, Capital Medical University, China between May 2017 and November 2021. We should note, some patients from our previous report[11] were also included in this study. The study was approved by the Ethics Committee of Xuanwu Hospital (NO.2016032) and written informed consent from all patients or their guardians was obtained before surgery.

Whole-exome sequencing and droplet digital PCR of human cavernous malformations

Human tissue samples obtained after resection were immediately transferred to the laboratory, snap-frozen in liquid nitrogen, and stored at −80°C. The frozen tissue samples were sent to the sequencing facility of Nanjing Geneseeq Biotechnology Inc. for whole-exome sequencing (WES) and ddPCR analyses. For WES, xGen Exome Research Panel v1.0 (Integrated DNA Technologies) was used for hybridization capture. The libraries were quantified by qPCR using a KAPA Library Quantification Kit (KAPA Biosystems) after target enrichment. Sequencing was performed on HiSeq4000 NGS platforms (Illumina) with paired-end 150 bp sequencing chemistry. We carried out ddPCR as previously reported.[24] Detection of rare variants in *MAP3K3* (NM_203351.1) and *PIK3CA* (NM_006218.2) was performed on the QX200 ddPCR system (Bio-Rad). Primers and probes for *MAP3K3* c.1416C>G p.Ile441Met were customized and synthesized at Integrated DNA Technologies (IDT) with the following nucleotide sequences: forward primer 5′-TCGTGCAGTACTAT GGCTGTC-3′, reverse primer 5′-TCACATGCATTCAAGGGGCA-3′, wild-type allele locked nucleic acid (LNA) probe 5′-HEX-TGAC CATCTTCAT-3′, mutant allele specific LNA probe 5′-FAM-TGAC CATGTTCAT-3′.

Infection of endothelial cells *in vitro* with lentiviruses

Human *MAP3K3*^{I441M} plasmids containing the open reading frames were amplified using primers with an added XhoI site on the 5′ end and a KpnI site on the 3′ end. PCR amplicons were then subcloned into GV141 using the XhoI/KpnI sites. *MAP3K3*^{I441M} cDNA fragment was cloned into the vector *pLJM1-EGFP*. These constructed plasmids were co-transfected into HEK293T cells, together with *psPAX2* and

pMD2.G using Lipofectamine 2000 reagent (Thermo). The lentiviruses were harvested after 24 h and then added to medium of bEnd.3 cells for 48-h culture with polybrene (10 μg/ml). The bEnd.3 cells with *MAP3K3*^{I441M} and EGFP stable co-expression were sorted via flow cytometry (BD FACSAria III) for subsequent bulk RNA sequencing.

Immunoprecipitation and western blot

HEK293T cells were cultured in Dulbecco's modified Eagle medium (DMEM, Cytiva) with 10% foetal bovine serum (FBS, Gibco) and 1% penicillin/streptomycin (Thermo Fisher Scientific) at 37°C in a 5% CO_2 incubator. jetPRIME DNA transfection reagents (Polyplus) were used for plasmids transfection. Forty-eight hours after transfection, cells were washed twice with PBS and incubated with lysis buffer, and then gently scraped into tubes. The incubation was on an end-over-end rotator for 1 h at 4°C. The lysis buffer includes 1% NP-40, 150 mM NaCl, 1 mM NaF, 50 mM Tris (pH 7.6) and protease inhibitor mixture (Roche). After centrifugation at 4°C at 12 000*g* for 10 min, the supernatants were collected and incubated with the primary antibody at 4°C overnight. The immune complexes were precipitated with prewashed protein A/G agarose beads (Beyotime) for 3.5 h at 4°C. The beads were washed six times. The SDS-PAGE buffer was then added and boiled at 95°C for 10 min. The following antibodies were used in the experiments: mouse anti-Myc (ABclonal, AE010), rabbit anti-Myc (ABclonal, AE070), and rabbit anti-HA (Abcam, Ab137838).

RNA sequencing and data analysis

Total RNA of endothelial cells was extracted with RNeasy Micro Kit (QIAGEN, Cat. No. 74004) as suggested by the manufacturer's protocol. RNA quality was measured with an Aglient RNA 6000 Pico kit. We used the RNA samples with RIN higher >8 for library preparation. The cDNA library was constructed using SMARTer® Stranded Total RNA-Seq Kit v2 (Takara).

Preprocessing and analysis of bulk RNA-seq

RNA-seq data were first subjected to 'FastQC' for data quality evaluation. Clean reads were mapped to the reference genome (Version: GRCm38) downloaded from Gencode by HISAT with the parameter '–5 30 –3 30'. Uniquely mapped reads were utilized to calculate the counts of each gene by feature counts with the parameter based on the GTF annotation downloaded from Gencode (Version: vm23). Read count matrix was normalized to library size by DESeq2 with default parameters. Hierarchical clustering was performed by factoextra package in R. Volcano plots were generated using the ggplot2 package in R, with cut-off of adjusted *P*-value < 0.01 and $\log_2$(fold change) absolute value >1.5, measured by DESeq2. The heat map was generated by pheatmap with the *z*-score of each gene. Gene set enrichment analysis (GSEA) was performed using the cluster Profiler package in R, with adjusted *P*-value < 0.05.

Drug administration

Rapamycin (APExBIO, A8167) was dissolved in DMSO (10 mg/ml, stock solution) and stored below –20°C. It was diluted with sterile saline before use (working concentration, 0.4 mg/ml). Mice were administered rapamycin (4 mg/kg body weight per day) via intraperitoneal injection (i.p.) starting on the second day or 2 weeks after AAV injection and continuing daily for 4 weeks. Brains of all animals underwent MRI scanning on the second and fourth weeks after drug injection. The brains of these mice were harvested during the fourth week after MRI scanning.

EdU staining

5-Ethynyl-2'-deoxyuridine (EdU) was dissolved with saline (2 mg/ml, working solution) and stored at –20°C. Mice were administered EdU (6 mg/kg body weight) intraperitoneally once every 2 days after they received the AAV injection.

Tamoxifen preparation and treatment

Tamoxifen was dissolved with corn oil (10 mg/ml). Mice were administered tamoxifen (100 mg/kg body weight per day) for five consecutive days after they received the AAV injection.

Data analysis and statistics

Animals were grouped with randomization during the experiments. NIH ImageJ software was used to quantify the data of immunostaining analysis from confocal microscopy. All data were analysed with GraphPad Prism software and are presented as mean ± standard error of the mean (SEM). *P*-values were calculated using an unpaired two-sided Student's *t*-test, or one-way ANOVA. Two-sided $P < 0.05$ was considered statistically significant and are denoted as follows: $^{*}P < 0.05$; $^{**}P < 0.01$; $^{***}P < 0.001$.

Data availability

The authors confirm that the data supporting the findings of this study are available within the article and its Supplementary material. Derived data supporting the findings of this study are available from the corresponding author on request.

Results

MAP3K3^{I441M} drives cerebral cavernous malformation formation in mice of different ages

MAP3K3 encodes MEKK3, a CCM2 binding partner.[25] LOF mutations in any of the three *CCM1/2/3* genes activate MEKK3–KLF2/4 signalling and contribute to the development and progression of CCMs.[18,26,27] We recently detected somatic mutations of *MAP3K3* and *PIK3CA* in CCMs of human patients. Mutations in both genes were found mainly in endothelial cells.[11] To investigate the role of *MAP3K3* ^{I441M} in CCM formation *in vivo*, we intravenously injected vascular endothelial-targeting adeno-associated virus BR1 (AAV-BR1) carrying *MAP3K3*^{I441M} (AAV-BR1-CAG-*MAP3K3*^{I441M}-P2A-EGFP, i.e. AAV-*MAP3K3*^{I441M}) into mice on postnatal Day 35 (P35) (Fig. 1A). AAV-BR1-CAG-P2A-EGFP (i.e. AAV-EGFP) was used as the control vector (Supplementary Fig. 1). These mice were subjected to T_2 MRI once per week. MRI revealed no obvious microlesions at 1 week after AAV-*MAP3K3*^{I441M} injection. At 2 weeks post-injection, however, many intracranial lesions with low MRI signal were identified that resembled human CCMs. The number of the lesions increased significantly between the second and fourth week after AAV-*MAP3K3*^{I441M} administration, with the number plateauing during the fifth and sixth weeks (Fig. 1B–D). We further performed MRI in mice at 4 months after injection of the AAV-*MAP3K3*^{I441M}. We found that the number of the lesions increased between the second and fourth months, while no larger lesions were identified in the MRI, which indicated the *MAP3K3* GOF mutations cause quiescent CCMs after a prolonged exposure to *MAP3K3*^{I441M} (Supplementary Fig. 2). Notably, single mutations of *CCM1/2/3* or

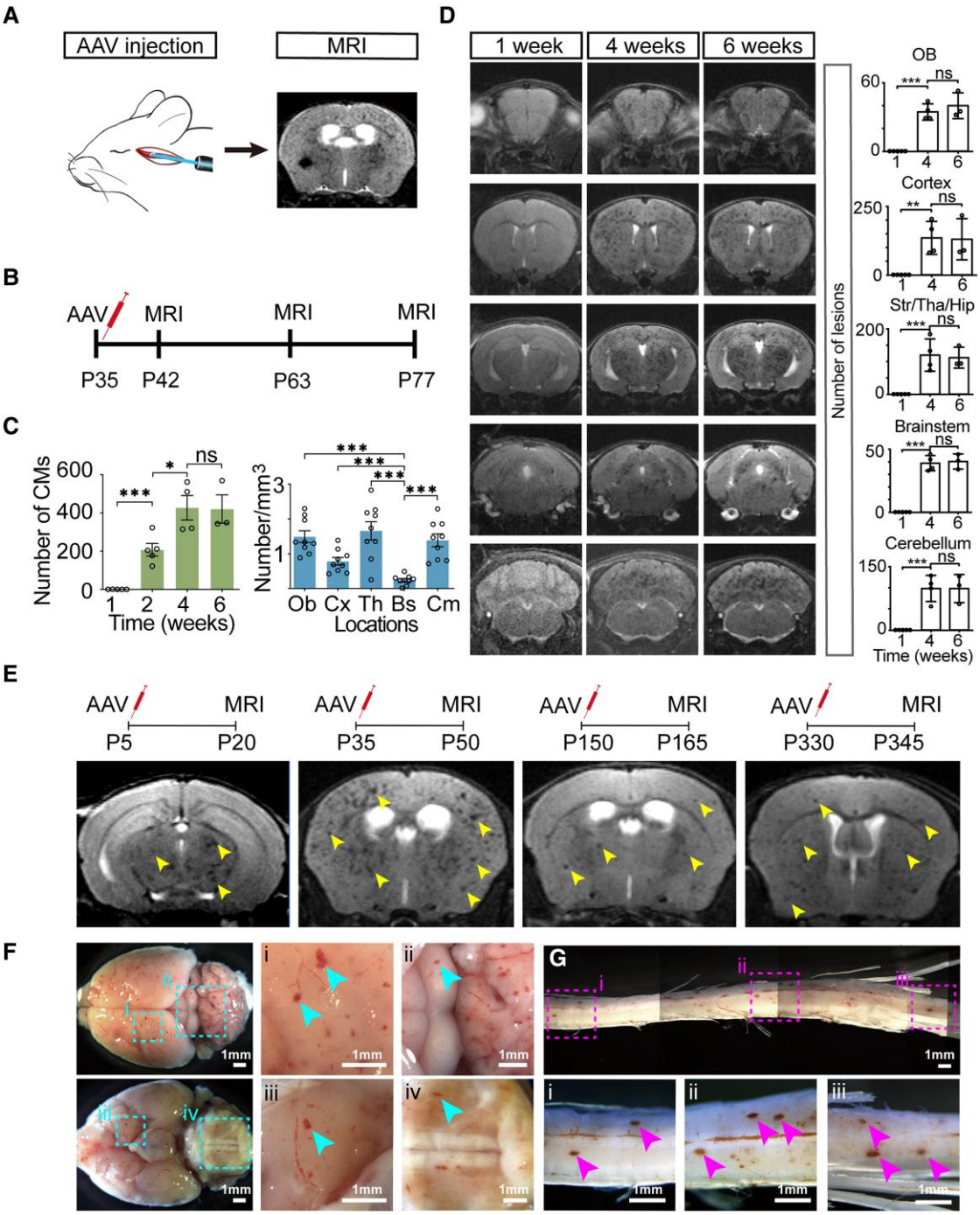

Figure 1 Formation of CCMs induced by *MAP3K3*^{I441M} mutations alone in mice of different ages. (**A**) Schematic of injection of AAV-BR1-*MAP3K3*^{I441M}-*P2A-EGFP* (i.e. AAV-*MAP3K3*^{I441M}) through the superficial temporal vein of a mouse. Regular T_2 MRI was used for CCM detection after aden-associated virus (AAV) injection. (**B**) Experimental design of a series of brain MRI in the mice infected with *MAP3K3*^{I441M}. (**C**) Quantification of the number of lesions in mouse brains in the first, second, fourth and sixth weeks after AAV injection. Compared with the data from the mice before AAV injection, no obvious difference in CCM numbers was identified in the first week ($n = 5$). In the second ($n = 5$) and fourth weeks ($n = 4$) after AAV-*MAP3K3*^{I441M} injection, the number of lesions increased significantly. The number of lesions reached a plateau in the sixth week after AAV injection ($n = 3$). The density of lesion in different brain regions. The number of lesions in the brainstem were significantly lower than that in other brain areas. Ob = olfactory bulb; Cx = cerebral cortex; Th = striatum, thalamus and hippocampus; Bs = brainstem; Cm = cerebellum. n.s. = not significant; $^{*}P < 0.05$; $^{***}P < 0.001$; one-way ANOVA. (**D**) Longitudinal T_2 MRI of different sections of a mouse brain at first, fourth and sixth weeks after injection of AAV-BR1-*MAP3K3*^{I441M}. Numerous microlesions were detected throughout the mouse brain. Quantification of the number of lesions in the MRI of different brain regions including olfactory bulb, cerebral cortex, striatum, thalamus and hippocampus, brainstem and cerebellum. MRI were performed at the first ($n = 5$ mice), fourth ($n = 4$ mice), and sixth ($n = 3$ mice) weeks. n.s. = not significant; $^{**}P < 0.01$; $^{***}P < 0.001$; one-way ANOVA. (**E**) Administration of AAV-*MAP3K3*^{I441M} in mice at different ages was essential to drive CCM formation in their brains and spinal cords. Mice aged P5, P35, P150 and P330 were injected with AAV-*MAP3K3*^{I441M} and T_2 MRI was performed 15 days later. MRI results showed that all mice of different ages developed CCMs in 2 weeks (arrowheads). (**F**) Example images of *MAP3K3*^{I441M} induced CCM lesions (arrowheads) in mice. AAVs were injected at P35 and brains were harvested at P50. [**F(i–iv)**] *Insets* from the brain. (**G**) Example images of *MAP3K3*^{I441M} induced spinal cord CM lesions (arrowheads). AAVs were injected at P35 and spinal cords were harvested at P50. [**G(i–iii)**] *Insets* from the spinal cord.

PIK3CA have not been reported to cause CCM lesions in the adult mouse brain.[15,17] Therefore, to further determine whether *MAP3K3*^{I441M} could drive lesion formation in both the developing and mature brain, we injected AAV-*MAP3K3*^{I441M} into mice at P5, P35, P150 and P330 (Fig. 1E) and then performed T_2 MRI 2 weeks after injection. Surprisingly, the lesions were distributed throughout the entire brain even in the P330 group (Fig. 1E). MRI showed that all mice developed lesions similar to human CCMs, regardless of the postnatal age at which they were injected (Fig. 1E). Dissection of each mouse brain and imaging with a stereoscope revealed numerous small vascular lesions located in both the brain and spinal cord (Fig. 1F and G and Supplementary Fig. 3). Staining of brain sections with H&E and Prussian blue revealed dilated vascular sinusoids lined by endothelial cells. Haemorrhages and staining for haemosiderin were observed around these lesions (Fig. 2A and B). Lesions were absent in the brain of control mice injected with AAV-EGFP. The *MAP3K3*^{I441M}-induced CCMs in mouse brain resembled *MAP3K3*^{I441M}-mutated CCMs in human patients (Fig. 2B). Together, these findings suggested that a single hit, i.e. *MAP3K3*^{I441M} mutation, can cause CMs in the brain and spinal cord of developing and adult mice. To determine what percentage of CCM patients having *MAP3K3*^{I441M} mutations alone or together with other mutations that have been reported in CCM patients, we systematically analysed all known CCM-related mutations in the WES results acquired for surgically resected CCM lesions from 104 patients (Supplementary Fig. 4A–D). These mutations included *MAP3K3* (p.I441M), *PIK3CA* (p.C378Y), *PIK3CA* (p.C420R), *PIK3CA* (p.E542K), *PIK3CA* (p.E545K), *PIK3CA* (p.H1047R), *AKT1* (p.E17K), *CCM1*, *CCM2* and *CCM3*, all of which have previously been found in CCM lesions.[11-13,15] The same patient-tissue samples were also analysed with ddPCR. The landscape of pathological mutations revealed that *MAP3K3*^{I441M} mutations were present in 45.2% of all CM lesions, including 57.3% of sporadic CMs, but were not seen in familial CMs. Of all *MAP3K3*^{I441M}-mutated CMs, 66.0% had no other known pathological mutations (Supplementary Fig. 4F–H). *MAP3K3*^{I441M}-mutated CMs occurred at comparable rates in male and female patients (57.4% and 42.6%, respectively; $n = 47$ in total). Interestingly, of all *MAP3K3*^{I441M} patients with CMs, 76.6% had SCCMs (Supplementary Fig. 4K). The patients with *MAP3K3*^{I441M} were distributed across a wide range of ages (mean ± SEM: 35.8 ± 2.2 years, range, 10–80 years old, $n = 47$ patients) (Supplementary Fig. 5L), but most were adults (87.2%, ≥18 years old). These results suggested that *MAP3K3*^{I441M} mutations are widely and exclusively present in sporadic CMs, mostly affecting adults. Together, these results illustrated that *MAP3K3*^{I441M} mutation alone—without any other known mutation—is a common genotype in sporadic CCMs and especially SCCMs. This strongly indicates that *MAP3K3*^{I441M} alone can induce CCMs in human patients, which is consistent with and supported by the results acquired with our CCM mouse model after administering AAV-*MAP3K3*^{I441M} (Fig. 1). Unlike other CCM-related mutations (i.e. to *CCM1*, *CCM3* and *PIK3CA*) reported previously,[15,17] our results for humans and mice strongly suggest that *MAP3K3*^{I441M} (i.e. one hit) can drive CCMs and SCCMs in both young and adult mice.

Time-lapse imaging of CCM formation in *MAP3K3*^{I441M} mice

To better understand the development of CCMs caused by *MAP3K3*^{I441M} *in vivo*, we used transcranial two-photon laser scanning microscopy (TPLSM) to analyse *NG2DsredBACtg* and *Pdgfrb-Cre*::*Ai14* mice after injection of AAV-*MAP3K3*^{I441M} at P35 (Fig. 3A). *NG2DsredBACtg* is a transgenic mouse line that is frequently used for labelling pericytes and smooth-muscle cells in the brain vasculature.[28,29] Daily imaging under a stereomicroscope revealed lesion formation in the superficial vasculature of the brain. The *de novo* vascular abnormalities appeared 2–3 weeks after AAV-*MAP3K3*^{I441M} injection (Fig. 3B), which was similar to the phenotype observed in patients (Supplementary Fig. 4B and C). To determine the distribution and alteration of blood flow in the cerebral vasculature in the CCM lesions, FITC-dextran dye was injected into the retro-orbital vein with subsequent analysis with time-lapse imaging via TPLSM. Massively bulged vascular caverns were observed in small vessels (Fig. 3C and D). Blood leakage was observed, reflecting a typical characteristic of CCMs in humans with *CCM1/2/3* mutations,[30-32] and dye leakage was also seen in the caverns of the *MAP3K3*^{I441M}-induced CCMs (Fig. 3F), indicating the disruption of the blood–brain barrier in the vasculature of CCM lesions. Interestingly, not all caverns leaked (8.9%, or $n = 16$ of 180 caverns) (Fig. 3H). Similar results were obtained with brain sections using endothelial cell-specific transgenic *Cdh5-CreER*::*Ai14* mice[33] after injection of AAV-*MAP3K3*^{I441M} (Fig. 2C and D). Pericytes have been reported to play a critical role in stabilizing newly formed capillaries[34] and in the maintenance of the blood–brain barrier.[35,36] The use of *NG2DsredBACtg* mice allowed us to measure the coverage of pericytes in normal and cavernous vessels. A low proportion of pericyte-free caverns was observed among the newly formed caverns (5.6%, $n = 10$ of 180 caverns; Fig. 3G). These results were confirmed in brain sections stained with anti-collagen IV in *Pdgfrb-Cre*::*Ai14* mice (Fig. 2E and F), another transgenic line in which pericyte labelling can be readily quantified.[37] To further investigate whether blood flow was altered in the vascular caverns induced by *MAP3K3*^{I441M}, we measured red blood cell velocity with line scanning under TPLSM. This analysis revealed both turbulent and stagnant blood flow in the caverns, which resembled the reduced perfusion of *MAP3K3*^{I441M}-mutated CCMs observed in patients (Fig. 3M–O and Supplementary Fig. 4C). Thus, long-term *in vivo* imaging of individual CCMs in the *MAP3K3*^{I441M} mouse brain revealed no significant alteration of pericyte coverage during the early stage of formation of vascular caverns. Also, leakage and alterations of blood flow were detected in vascular caverns.

MAP3K3^{I441M} initiates cerebral cavernous malformation formation without an obvious increase in endothelial cell proliferation

Previous studies have revealed that GOF of oncogenic *PIK3CA* somatic mutations drives excessive cell proliferation in CCMs.[15] To determine whether the GOF *MAP3K3*^{I441M} mutation initiates CCM formation via a similar mechanism, we used P35 *Cdh5-CreER*::*Ai14tg* mice as an experimental model. The mice were first infected with AAV-*MAP3K3*^{I441M}; after 4 days, they received a daily injection of EdU for 10 days to label dividing cells. After two additional days, an abundance of dividing cells (i.e. EdU$^+$) were detected in the subventricular zone of the brain, a site of pronounced neurogenesis. Interestingly, no dividing endothelial cells were found in the 50 *MAP3K3*^{I441M}-mutated CCMs that we imaged (0.0%, $n = 0$ of 50 lesions, 0.0%, $n = 0$/100 normal vessels) (Fig. 4A and B). We then carried out immunohistochemistry for Ki67, a cell proliferation marker, in human tissues of CCMs expressing *MAP3K3*^{I441M}. Ki67$^+$ endothelial cells were rarely detected in CCM tissue (Fig. 4C and D, $n = 2$ patients). These results suggested that endothelial cell proliferation is likely not the main driving force for initiation of vascular caverns, which is consistent with our results obtained for human CCMs.

To further determine how *MAP3K3*^{I441M} alters endothelial cells and causes vascular CMs, we compared the size of endothelial cells

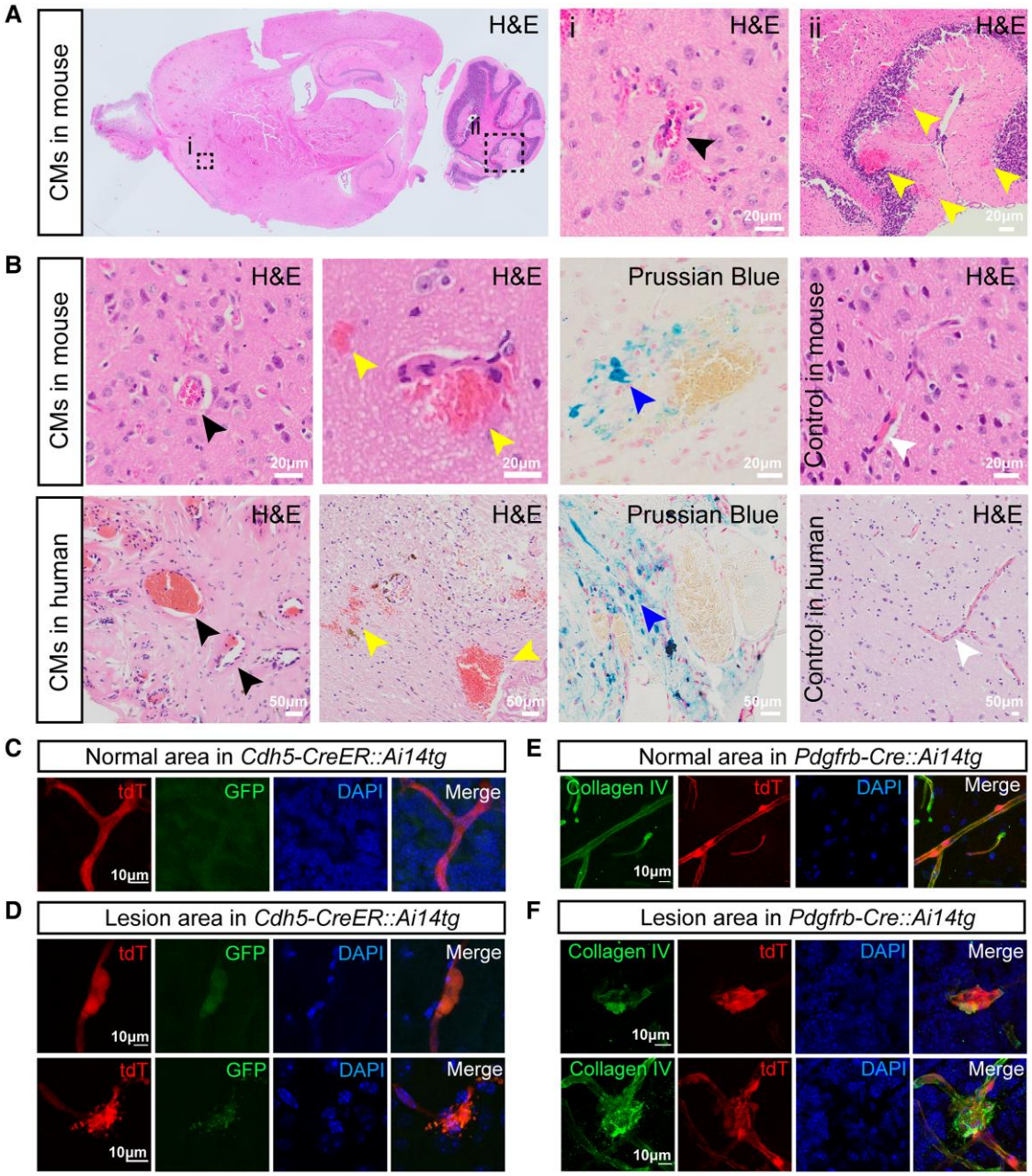

Figure 2 Characteristics and morphology of MAP3K3^{I441M} -induced CCM lesions. (**A**) Representative images of H&E staining of MAP3K3^{I441M} -induced CCM lesions (arrowhead, *inset* **i**) and haemorrhage (arrowheads, *inset* **ii**) in mice. (**B**) Characteristics of MAP3K3^{I441M}-induced CCM lesions and the control blood vessels in mouse brains (*top*), and characteristics of CCM lesions from a patient with MAP3K3^{I441M} mutations (*bottom*). H&E staining (lesions, arrowheads in first panel; haemorrhage, arrowheads in second panel) and iron deposits of haemosiderin (patches, arrowheads in third panel) in MAP3K3^{I441M}-induced CCM lesions from mice or brain tissue from human patients. Dilated vascular sinusoids were lined by endothelial cells (arrowheads in first panel). Haemorrhages and haemosiderin stains surrounded the lesions (second and third panels). The images from control groups are shown in the fourth panel. (**C** and **D**) The morphology of CMs induced by MAP3K3^{I441M} in *Cdh5-CreER::Ai14tg* mice. Example images of brain sections from *Cdh5-CreER::Ai14tg* mice injected with AAV-BR1-MAP3K3^{I441M}-*P2A-EGFP*. Representative images of MAP3K3^{I441M}-induced CM lesions with dilated lumen (*top*, **D**) or distorted lumen (*bottom*, **D**). Tdt = tdTomato signal (red) in endothelial cells from *Cdh5-CreER::Ai14tg*; nuclei, DAPI (blue); GFP = weak green signal from endothelial cells (green) infected by AAV-BR1-MAP3K3^{I441M}-*P2A-EGFP*. (**E** and **F**) The morphology of CMs induced by MAP3K3^{I441M} in *Pdgfrb-Cre::Ai14tg* mice. Example images of brain sections stained with anti-Collagen IV in *Pdgfrb-Cre::Ai14tg* mice 2 weeks after infection with AAV-BR1-MAP3K3^{I441M}. Normal blood vessels in brain region (**E**). Representative images of MAP3K3^{I441M}-induced CM lesions with dilated lumen (**F**). Blood vessels, collagen IV (green); nuclei, DAPI (blue), and tdT signal (red) from pericytes in *Pdgfrb-Cre::Ai14tg* mice.

of MAP3K3^{I441M}-induced vascular caverns with the size of those in normal capillaries. Interestingly, the area of individual endothelial cells expressing MAP3K3^{I441M} was significantly larger than that of individual cells lacking MAP3K3^{I441M} expression (Fig. 4F–H). Autophagic degradation is crucial for cell survival.[38] We stained blood vessels with p62, a marker for autophagy and observed many p62 bodies surrounding caverns of blood vessels in mice with AAV-MAP3K3^{I441M} infection (Supplementary Fig. 5). We also

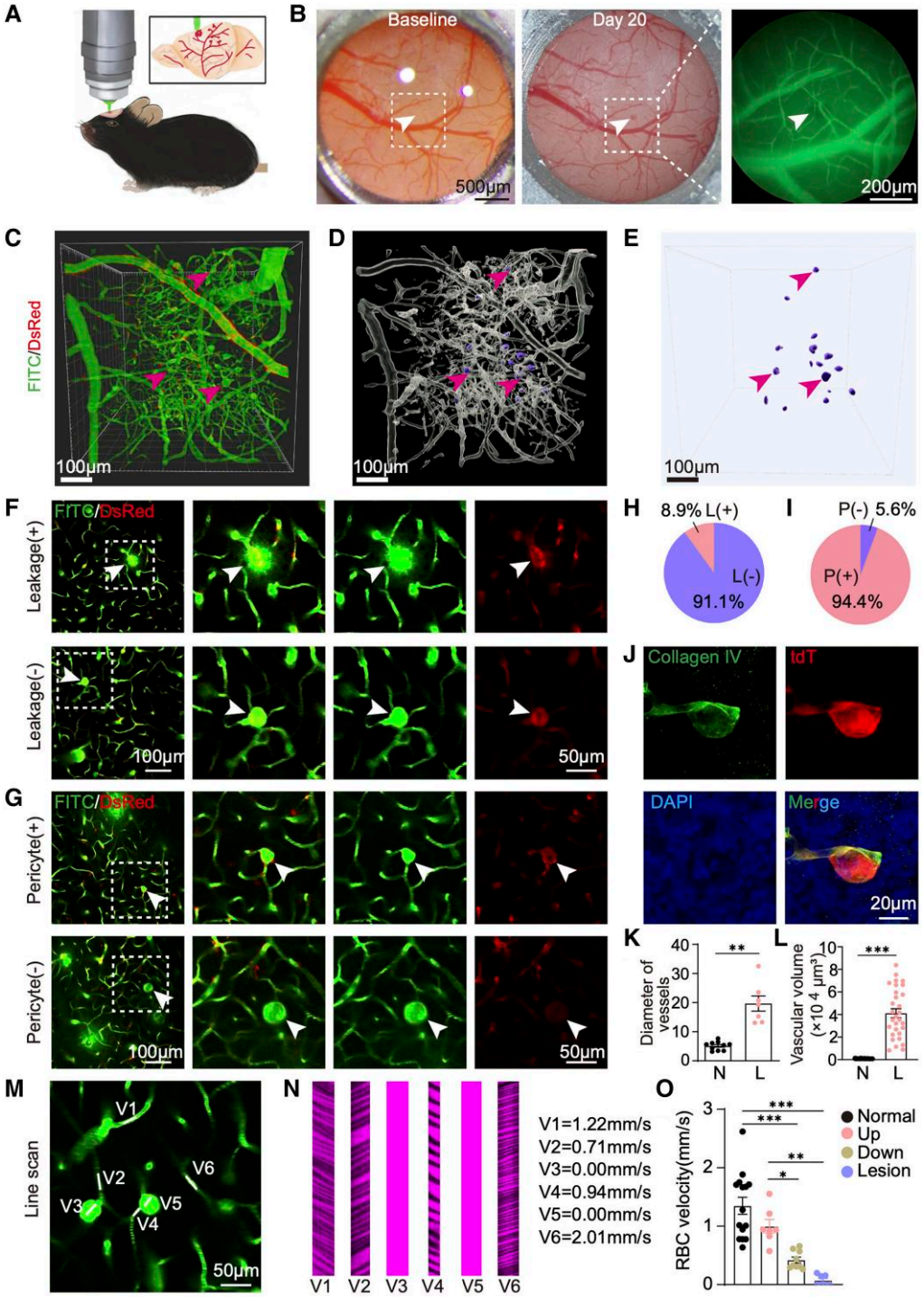

Figure 3 ***In vivo*** **imaging of the development of CCMs caused by** ***MAP3K3***^{I441M}. (**A**) Schematic of time-lapse live imaging of the brain vasculature in a conscious mouse. (**B**) Imaging of the development of a CCM lesion (arrowheads) located in a mouse brain through a chronic cranial window. Before AAV injection (baseline, *left*); 20 days after AAV injection (Day 20, *middle*). *Inset*: The same region within the dashed box with FITC-dextran (green) circulating in blood vessels (*right*). (**C–E**) Three-dimensions of a z-stack image taken by a two-photon laser excitation microscope. Green = FITC-dextran; red = Dsred signal in the *NG2BacDsRed* transgenic(tg) mouse. (**F–H**) CCM lesions (*arrowheads*) with leakage (*top*) and without leakage (*bottom*) in *NG2BacDsRed* tg mouse (**F**). Percentage of CCM lesions with leakage ($n = 180$ lesions in total). L(+) = leakage; L(–) = with no leakage (**H**). (**G–I**) A CCM lesion (arrowheads) with coverage of pericytes (*top*) and without coverage of pericytes (*bottom*). (**I**) The percentage of lesions with pericyte [P(+)] or without pericyte coverage [P(–)]($n = 180$ lesions in total). (**J**) The coverage of pericytes in individual CCMs mediated by *MAP3K3*^{I441M} mutations from the brain of *Pdgfrb-Cre::Ai14 tg*. Blood vessels were stained with antibodies against Collagen IV (green). Nuclei were stained with DAPI (blue). (**K** and **L**) Diameter and volume of the CCM lesions and normal vessels; $^{*}P < 0.05$; $^{**}P < 0.01$; $^{***}P < 0.001$; one-way ANOVA. (**M–O**) Characterization of blood flow in individual CCMs induced by *MAP3K3*^{I441M} mutations. Positions of line scanning in normal vessels (V1, V6), parent vessels (V2, V4) and cavernous vessels of CCM lesions (V3, V5). (**N**) The velocity of blood cells in vessels shown in (**M**) measured through line scanning. Images were plotted with *X-T* mode (the y-axis represents time and the x-axis represents distance) in the locations of V1 to V6. (**O**) Summarized results of red blood cell velocities in the upstream (Up, $n = 7$) and downstream (Down, $n = 9$) of the parent vessels, in normal blood vessels ($n = 15$), and in cavernous vessels of CCM lesions ($n = 7$), one-way ANOVA and $^{*}P < 0.05$, $^{**}P < 0.01$, $^{***}P < 0.001$.

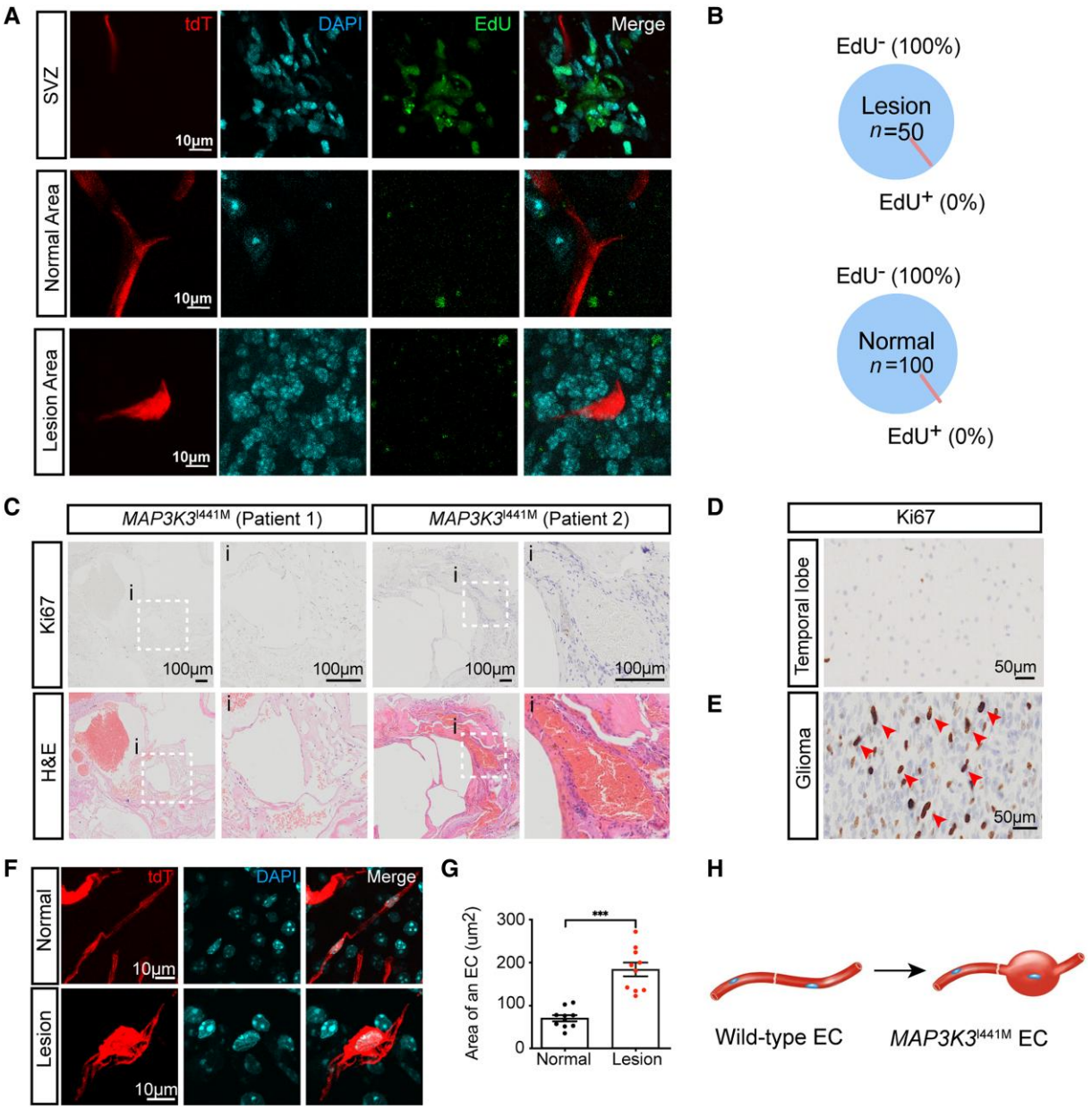

Figure 4 Staining of endothelial cell proliferation in tissues from MAP3K3^{I441M} mouse models and CCM human samples. (**A**) Cell proliferation assays (EdU) in *Cdh5-CreER::Ai14tg* mice 2 weeks after infected with AAV-BR1-*MAP3K3*^{I441M}. EdU positive cells (green, third row) were detected in the subventricular zone (SVZ), a neurogenic region in the brain. (**B**) No EdU^{+} endothelial cells were detected in *MAP3K3*^{I441M}-mutated CCMs (0.0%, $n = 0/50$ lesions in total) or in normal vessels (0.0%, $n = 0/100$ normal vessels in total). (**C**) H&E staining and Ki67 staining in CCMs of human with *MAP3K3*^{I441M} mutations. No positive immunoreaction for Ki67 was observed. (**i**) *Insets* from H&E staining in **C**. (**D**) Ki67 staining in the 'control' tissue (without CCMs) of the temporal lobe from an epilepsy patient. No positive immunoreaction for Ki67 was observed. (**E**) Ki67 staining in the tissue of human glioma. (**F**) Example images of normal capillaries and *MAP3K3*^{I441M} mutated CCMs in *Cdh5-CreER::Ai14* mice after injection of AAV- *MAP3K3*^{I441M}. DAPI (blue) and tdTomato (tdT, red) signal from endothelial cells in *Cdh5-CreER::Ai14tg*. (**G**) Comparison of the membrane area of single endothelial cell of *MAP3K3*^{I441M} induced CCMs ($n = 10$) with that of normal capillaries ($n = 10$) in *Cdh5-CreER::Ai14* mice after injection of AAV- *MAP3K3*^{I441M}. ***$P < 0.001$, unpaired two-tailed Student's *t*-test. (**H**) Schematic of the morphology of endothelial cells with *MAP3K3*^{I441M} expression and without *MAP3K3*^{I441M} expression.

detected there were higher cleaved caspase-3 signals in blood vessels of *MAP3K3*^{I441M}-induced vascular caverns (Supplementary Fig. 6).

mTOR pathway is activated in endothelial cells expressing *MAP3K3*^{I441M}

To further explore the underlying molecular pathways altered by *MAP3K3*^{I441M} in endothelial cells, the mouse endothelial cell line bEnd.3 was first infected with lentivirus-*MAP3K3*^{I441M} (LV-*MAP3K3*^{I441M}-*P2A-EGFP*; LV-EGFP was used as the control). Total RNA from these cells was then subjected to RNA sequencing. The transcriptome of the *MAP3K3*^{I441M}-expressing cells differed significantly from that of the control cells (Fig. 5A–E and Supplementary Fig. 7). Considering that *MAP3K3*^{I441M} mutations increase the size of the plasma membrane of individual endothelial cells, GSEA was carried out, revealing upregulation of the structural constituent of cytoskeleton pathway in *MAP3K3*^{I441M}-expressing endothelial cells (Fig. 5C

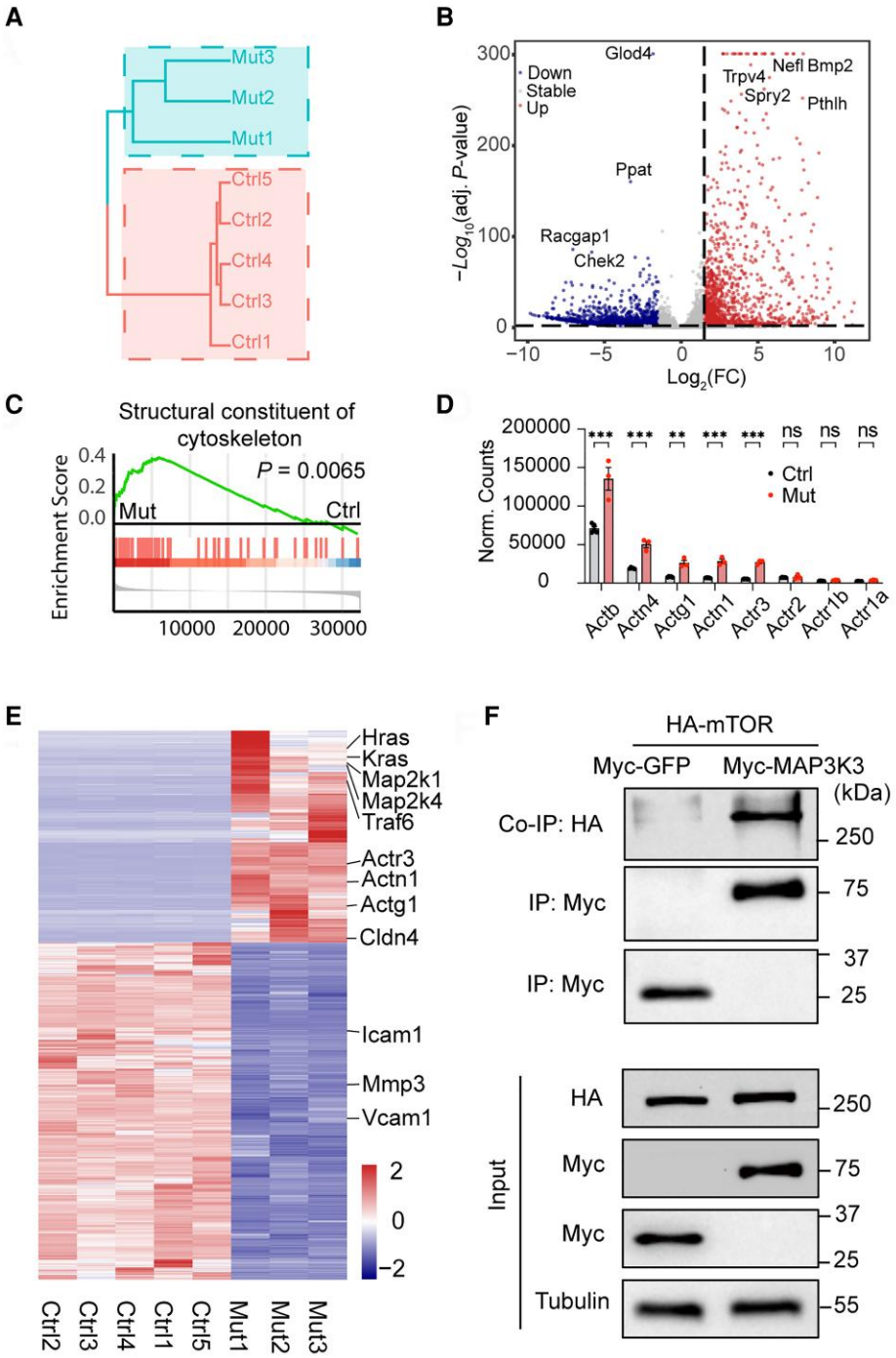

Figure 5 Molecular mechanism of the induction of CCMs by *MAP3K3*^{I441M}. (**A**) Hierarchical cluster of all samples of bulk RNA-sequencing from brain endothelial cell lines, bEnd.3. Three samples from endothelial cells with lentivirus-*MAP3K3*^{I441M} infection (Mut 1–3) and five control samples with lentivirus-*EGFP* infection (Ctrl 1–5). (**B**) Downregulated (blue) and upregulated (red) genes [$\log_2$ fold-change (FC) > 1.5, adjusted *P*-value < 0.05] in the endothelial cells with expression of *MAP3K3*^{I441M}. (**C**) GSEA showed the activated pathway of structural constituent of cytoskeleton in the endothelial cells with *MAP3K3*^{I441M} expression. (**D**) Normalized counts of the top eight genes encoding actins in bulk RNA-sequencing data acquired from the control endothelial cells ($n = 5$) and those cells with *MAP3K3*^{I441M} expression ($n = 3$). ***$P < 0.001$, unpaired two-tailed Student's *t*-test. (**E**) The heat map showing the *z*-scores of normalized counts for differential genes, as measured by bulk RNA-Sequencing. Some featured genes (e.g. *Traf6*, *Actn1*, etc.) were highlighted. (**F**) Western blot results for demonstrating MAP3K3-mTOR interactions. Co-immunoprecipitation (IP) results showed MAP3K3 interacted with mTOR.

and Supplementary Fig. 7). Among the top eight most enriched actin-encoding genes in endothelial cells, five *ACT* genes were upregulated in cells expressing *MAP3K3*^{I441M}. Previous results reported that MAP3K3 regulates the phosphorylation of p62 and promotes mTOR activation.[39] Pull-down experiments were performed in cells with overexpression of three different constructs, Myc-GFP, HA-mTOR, and Myc-MAP3K3. We also performed co-immunoprecipitation experiments in two groups of cells co-transfected with

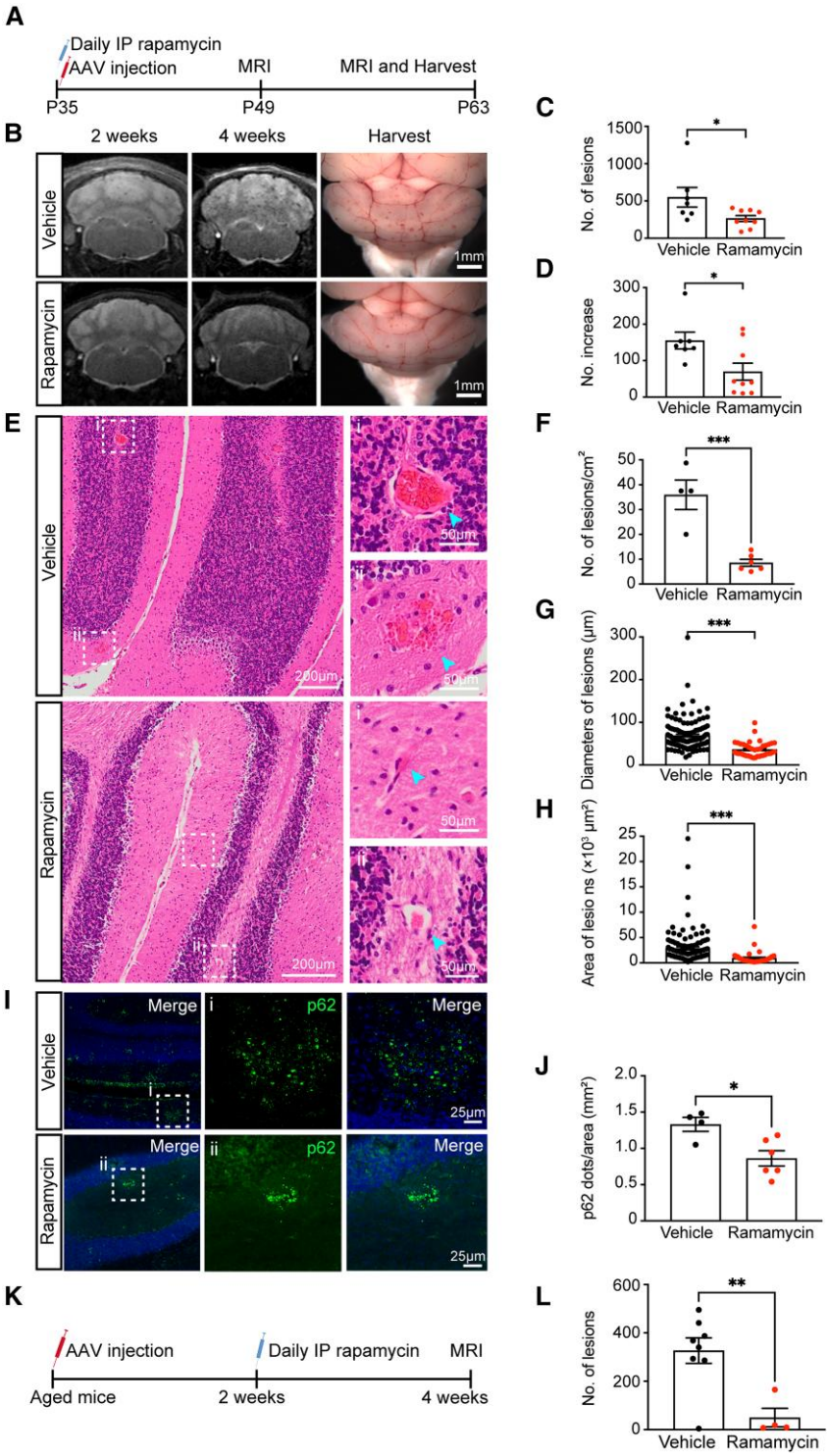

Figure 6 Blocking mTOR activity with rapamycin prevents progression of *MAP3K3*^{I441M}-mediated formation of CCMs. (**A**) Experimental design for our strategy of the targeted therapy using mTOR inhibitor rapamycin in mice with *MAP3K3*^{I441M} CCMs. (**B**) T_2 MRI of mouse brains after treatment using rapamycin or vehicle at the second and fourth week, and visual images of the hindbrains of mice treated by rapamycin or vehicle for 4 weeks. Scale bars = 1 mm. (**C**) Quantification of the number of CCM lesions in mice with and without the rapamycin treatment. Vehicle group, $n = 7$ mice; rapamycin, $n = 9$ mice; $^{*}P < 0.05$, unpaired two-sided Student's *t*-test. (**D**) Quantification of the increase of CCM lesion numbers between the second and fourth week after the treatment with vehicle or rapamycin. Vehicle, $n = 7$ mice; rapamycin, $n = 9$ mice; $^{*}P < 0.05$, unpaired two-sided Student's *t*-test. (**E**) H&E staining of mouse brains after treatment using rapamycin or vehicle at the fourth week (lesions, arrowheads). (**i** and **ii**) *Insets* from H&E staining in **E**. (**F**–**H**) Quantification of CCM: the density of lesions (**F**), the diameter of lesions (**G**), and the area of a single lesion (**H**) with H&E staining at the fourth week in vehicle or rapamycin-treat CCM mice. $^{***}P < 0.001$, unpaired two-tailed Student's *t*-test. (**I**) Autophagy marker, p62 staining of the brain sections from mice treated with rapamycin or vehicle for 4 weeks. (**J**) The number of p62 bodies was significantly decreased in the rapamycin-treated group. $^{*}P < 0.05$, unpaired two-tailed Student's *t*-test. (**K**) Experimental design for our strategy of the targeted therapy using mTOR inhibitor rapamycin in aged mice (18–24 months) with *MAP3K3*^{I441M} CCMs. (**L**) Quantification of the number of CCM lesions in aged mice in vehicle or rapamycin-treated groups. Vehicle group, $n = 8$ mice; rapamycin, $n = 4$ mice; $^{**}P < 0.01$, unpaired two-tailed Student's *t*-test.

HA-mTOR plus Myc-GFP, and HA-mTOR plus Myc-MAP3K3, repectively. Proteins were pulled down with the Myc antibody. We found that Myc-MAP3K3 interacts with mTOR directly. These results indicated that MAP3K3 activation increases the activity of the mTOR pathway, which provides direct evidence for how blocking mTOR with rapamycin alleviates symptoms in mice with *MAP3K3*^{I441M}-induced CCMs (Fig. 5F). The results of the transcriptomic analysis implied that *MAP3K3*^{I441M} can activate the mTOR pathway, leading to alterations of the cytoskeleton before cavern formation in the brain.

Blocking mTOR activity with rapamycin prevents progression of *MAP3K3*^{I441M}-mediated formation of cerebral cavernous malformations

Rapamycin is an mTOR inhibitor that has been approved by the US Food and Drug Administration. As such, rapamycin is a promising agent for targeted pharmacological management of vascular malformations.[15,40,41] To test whether blocking the mTOR pathway could slow the formation of CCMs, rapamycin was administered to mice with *MAP3K3*^{I441M}-induced CCMs. The fact that the mTOR pathway was activated in endothelial cells expressing *MAP3K3*^{I441M} (Fig. 5) suggested that rapamycin might mitigate CCM formation in *MAP3K3*^{I441M} mice. Mice injected with AAV-*MAP3K3*^{I441M} were treated with rapamycin (4 mg/kg, i.p. injection) or vehicle control daily for 4 weeks. All animals underwent MRI at 2 and 4 weeks after AAV injection. At the 4-week time point, each brain was imaged and harvested (Fig. 6A). The results of MRI and H&E staining of the brain sections revealed that 4 weeks of rapamycin treatment significantly decreased the number of CCM lesions (Fig. 6B–H), suggesting that blocking mTOR with rapamycin might be an effective therapeutic option for *MAP3K3*^{I441M}-driven sporadic CCMs. To further verify our results, we also stained the section with p62, a marker for autophagy. The number of p62 bodies significantly decreased in rapamycin-treated mouse group (Fig. 6I and J). As sporadic CMs with *MAP3K3*^{I441M} mutations are usually found in adult patients, to further test whether rapamycin treatment works on mice after caverns are formed, we infected the aged mice (age, 18–24 months old) with AAV-*MAP3K3*^{I441M} for 2 weeks before we treated these mice with rapamycin (Fig. 6K). We observed that rapamycin could also substantially inhibit the progression of CCM formation after a prolonged exposure with *MAP3K3*^{I441M} in these mice (Fig. 6L). We performed pathological analyses (staining for autophagy, microlesion/bleeding and apoptosis) between the vehicle and rapamycin-treated mice. We found that rapamycin significantly alleviated the symptoms in mice with *MAP3K3*^{I441M}-induced CCMs. The density and size of microlesions decreased in the brain sections of rapamycin-treated groups. Furthermore, we also detected that the number of autophagy bodies decreased dramatically in rapamycin-treated mice. We treated the *MAP3K3*^{I441M} CCM mice with ponatinib (AP24534), a blocker for MAP3K3. However, we detected severe side effects in survival, body weight and neurological behaviours in both CCM and wild-type mice. Thus, we did not continue the treatments.

Discussion

Both CCMs and SCCMs are common vascular abnormalities of the CNS. They are major causes of stroke, seizures and neurological deficits. Activating, single somatic mutations in the RAS–MAPK pathway have been reported to drive arteriovenous malformations.[42,43] Although multiple genes may contribute to CCM formation, no reported single gene variant has been demonstrated to be sufficient for CCM induction in an adult mouse model.[15,17] Thus, previous accounts mainly proposed two-hit hypotheses involving biallelic LOF via *CCM1/2/3* mutations or a three-hit hypothesis including both *CCM1/2/3* LOF and *PIK3CA* GOF.[5–7,15] In mice, CCMs have only been observed when LOF of *CCM1/2/3* or GOF of *PIK3CA* occurs in early postnatal stages. After P21, CCM phenotypes are rare in the mouse brain, typically occurring only when *CCM1/2/3* LOF and *PIK3CA* GOF co-exist in the same endothelial cells.[15] Unlike *CCM1/2/3*- and *PIK3CA*-induced CCMs, *MAP3K3*^{I441M} mutations alone were widely identified in our patient cohort with sporadic CCMs and SCCMs (Fig. 3). This strongly suggests that a one-hit mechanism (i.e. *MAP3K3* →*MAP3K3*^{I441M}) may underlie the formation of CCMs, and this is supported by results from our mouse model of CCM. The introduction of *MAP3K3*^{I441M} mutations into mice at age P5, P35, P150 and P330 caused CMs in the brain or spinal cord. These results demonstrate that expression of *MAP3K3*^{I441M} specifically in endothelial cells of the brain or spinal cord is sufficient to drive CCM formation with dilated, low-flow leaky caverns (i.e. CCM lesions) in adult mice. Interestingly, our EdU pulse-chase experiment with mice did not reveal an obvious increase in endothelial-cell proliferation in CCM lesions. We conclude that the mechanism of *MAP3K3*^{I441M}-mediated CCM formation differs from that expected based on the simple activation of MEKK3 downstream signalling pathways,[11,12] but this conclusion must be confirmed in a future study.

In mice expressing *MAP3K3*^{I441M}, the number of brain lesions is higher with respect to spinal cord CCMs while the opposite has been observed in CMs collected by patients.[11,44] Based on our clinical experience and observation of >100 patients with *MAP3K3* mutation at Xuanwu Hospital, the patients with *MAP3K3*^{I441M} mutation have a lower likelihood of bleeding in the CNS than patients without this specific mutation. Since *MAP3K3*^{I441M} patients do not have severe symptoms in the brain, they tend not to see doctors. As a result, these patients with micro-lesions in the brain have a lower probability of being diagnosed in hospitals than those with CCM lesions in the spinal cord. Since the spinal cord is directly involved in various sensory functions, small lesions in the spinal cord caused by *MAP3K3*^{I441M} mutation have a higher potential to cause symptoms that are bothersome to patients.

Understanding the mechanism underlying the initiation of *MAP3K3*^{I441M}-induced sporadic CCMs is crucial for developing new therapies for the ∼40% of CCM patients with this mutation. Previous reports have posited various explanations for CCMs and proposed that they are likely congenital lesions.[45,46] The lifetime risk of haemorrhage has been underestimated. Our animal model, which takes into account postnatal age at CCM onset, will prompt a rethinking of how sporadic CCMs form. This animal model will also provide the CCM research community with a means for studying lesion development, haemorrhage onset, and the occurrence of other symptoms, such as seizures, in patients with sporadic CCMs.

Surgical resection remains the only treatment for most CCMs, as no pharmacological option currently exists.[47] However, resection carries the risk of surgical complication and is extremely challenging for lesions located in deep-brain regions; consequently, morbidity and mortality rates are non-negligible.[3,47] Recent studies have reported that somatic *MAP3K3* mutations activate MAP3K3 downstream signalling pathways.[11,12] The consequent increase in CCM–MAP3K3–KLF2/4 signalling upregulates PI3K–mTORC1 signalling, and hence rapamycin can prevent CCM lesion formation stemming from *CCM1/2/3* LOF and *PIK3CA* GOF.[15] Somatic mutation *MAP3K3*^{I441M} is common in sporadic CCMs and SCCMs and it has

been shown as a GOF mutation. This GOF mutation in *MAP3K3* has been proposed to have similar functional consequences of LOF mutations in CCM genes.[48] It was also reported that the *MAP3K3 GOF* mutation causes quiescent CCM.[49] Our results reveal that *MAP3K3*^{I441M} mutations drive the formation of CCMs and SCCMs via activation of MAPK and mTOR signalling in endothelial cells and altering the cytoskeleton. Furthermore, our RNA sequencing results demonstrate that MAP3K3 can interact with mTOR directly, although LV-*MAP3K3*^{WT}-*P2A-EGFP* is a more reasonable control for the mutant protein. Since we could not treat CCM mice with MAP3K3 inhibitor ponatinib (AP24534) for a longer time, we could not evaluate its effect.

Our results also demonstrate that *MAP3K3*^{I441M}-induced CCMs can be prevented by treatment with the mTOR inhibitor rapamycin. These results provide insights into the pathogenesis of sporadic CCM and suggest a therapeutic alternative.

Acknowledgements

We thank Xinwei Gao, Mingyue Jia, and Dr Qingchun Guo from CIBR Imaging facility, Yingzi Ju from CIBR Vector Core, Jingmei Chen and Dr Li Zhang from Genomics Center, Shufang Huang and Dr Wenlong Li from CIBR Laboratory Animal Resource Center for their support. We thank the lab members at Sun and Ge lab and colleagues from Chinese Institute for Brain Research, Beijing for discussion. Dr Bridget Samuels for critical reading.

Funding

This work is supported by National Natural Science Foundation of China with grant (No. 32170964) and CIBR start-up funds to W-P.G., grant (No.81971104) to T.H., grant (No. 82201440) to J.R., and grant (No. 81971113) to H.Z.; Beijing Municipal Science and Technology Commission with grant Z201100005520024 to T.H. Beijing Municipal Administration of Hospitals with grant DFL20180801 to H.Z. and QML20190802 to T.H. Beijing Municipal Education Commission with grant CIT&TCD201904095 to T.H.

Competing interests

The authors report no competing interests.

Supplementary material

Supplementary material is available at *Brain* online.

References

1. Vernooij MW, Ikram MA, Tanghe HL, *et al*. Incidental findings on brain MRI in the general population. *N Engl J Med*. 2007;357:1821-1828.
2. Morris Z, Whiteley WN, Longstreth WT Jr, *et al*. Incidental findings on brain magnetic resonance imaging: Systematic review and meta-analysis. *BMJ*. 2009;339:b3016.
3. Batra S, Lin D, Recinos PF, Zhang J, Rigamonti D. Cavernous malformations: Natural history, diagnosis and treatment. *Nat Rev Neurol*. 2009;5:659-670.
4. Chohan MO, Marchio S, Morrison LA, *et al*. Emerging pharmacologic targets in cerebral cavernous malformation and potential strategies to Alter the natural history of a difficult disease: A review. *JAMA Neurol*. 2019;76:492-500.
5. Laberge-le Couteulx S, Jung HH, Labauge P, *et al*. Truncating mutations in CCM1, encoding KRIT1, cause hereditary cavernous angiomas. *Nat Genet*. 1999;23:189-193.
6. Liquori CL, Berg MJ, Siegel AM, *et al*. Mutations in a gene encoding a novel protein containing a phosphotyrosine-binding domain cause type 2 cerebral cavernous malformations. *Am J Hum Genet*. 2003;73:1459-1464.
7. Bergametti F, Denier C, Labauge P, *et al*. Mutations within the programmed cell death 10 gene cause cerebral cavernous malformations. *Am J Hum Genet*. 2005;76:42-51.
8. Cox EM, Bambakidis NC, Cohen ML. Pathology of cavernous malformations. *Handb Clin Neurol*. 2017;143:267-277.
9. Zafar A, Quadri SA, Farooqui M, *et al*. Familial cerebral cavernous malformations. *Stroke*. 2019;50:1294–1301.
10. Flemming KD, Graff-Radford J, Aakre J, *et al*. Population-Based prevalence of cerebral cavernous malformations in older adults: Mayo clinic study of aging. *JAMA Neurol*. 2017;74:801-805.
11. Hong T, Xiao X, Ren J, *et al*. Somatic MAP3K3 and PIK3CA mutations in sporadic cerebral and spinal cord cavernous malformations. *Brain*. 2021;144:2648-2658.
12. Weng J, Yang Y, Song D, *et al*. Somatic MAP3K3 mutation defines a subclass of cerebral cavernous malformation. *Am J Hum Genet*. 2021;108:942-950.
13. Peyre M, Miyagishima D, Bielle F, *et al*. Somatic PIK3CA mutations in sporadic cerebral cavernous malformations. *N Engl J Med*. 2021;385:996-1004.
14. Snellings DA, Girard R, Lightle R, *et al*. Developmental venous anomalies are a genetic primer for cerebral cavernous malformations. *Nat Cardiovasc Res*. 2022;1:246-252.
15. Ren AA, Snellings DA, Su YS, *et al*. PIK3CA And CCM mutations fuel cavernomas through a cancer-like mechanism. *Nature*. 2021;594:271-276.
16. Akers AL, Johnson E, Steinberg GK, Zabramski JM, Marchuk DA. Biallelic somatic and germline mutations in Cerebral Cavernous Malformations (CCMs): Evidence for a two-hit mechanism of CCM pathogenesis. *Hum Mol Genet*. 2009;18:919-930.
17. Zhou HJ, Qin L, Jiang Q, *et al*. Caveolae-mediated tie2 signaling contributes to CCM pathogenesis in a brain endothelial cell-specific Pdcd10-deficient mouse model. *Nat Commun*. 2021;12:504.
18. Zhou Z, Tang AT, Wong WY, *et al*. Cerebral cavernous malformations arise from endothelial gain of MEKK3-KLF2/4 signalling. *Nature*. 2016;532:122-126.
19. Maddaluno L, Rudini N, Cuttano R, *et al*. EndMT contributes to the onset and progression of cerebral cavernous malformations. *Nature*. 2013;498:492-496.
20. Tang AT, Choi JP, Kotzin JJ, *et al*. Endothelial TLR4 and the microbiome drive cerebral cavernous malformations. *Nature*. 2017;545:305-310.
21. Korbelin J, Dogbevia G, Michelfelder S, *et al*. A brain microvasculature endothelial cell-specific viral vector with the potential to treat neurovascular and neurological diseases. *EMBO Mol Med*. 2016;8:609-625.
22. Jia JM, Peng C, Wang Y, Zheng J, Ge WP. Control of occlusion of middle cerebral artery in perinatal and neonatal mice with magnetic force. *Mol Brain*. 2018;11:47.
23. Jia JM, Chowdary PD, Gao X, *et al*. Control of cerebral ischemia with magnetic nanoparticles. *Nat Methods*. 2017;14:160-166.
24. Hong T, Yan Y, Li J, *et al*. High prevalence of KRAS/BRAF somatic mutations in brain and spinal cord arteriovenous malformations. *Brain*. 2019;142:23-34.
25. Fisher OS, Deng H, Liu D, *et al*. Structure and vascular function of MEKK3-cerebral cavernous malformations 2 complex. *Nat Commun*. 2015;6:7937.
26. Cuttano R, Rudini N, Bravi L, *et al*. KLF4 Is a key determinant in the development and progression of cerebral cavernous malformations. *EMBO Mol Med*. 2016;8:6-24.

27. Castro M, Lavina B, Ando K, *et al*. CDC42 Deletion elicits cerebral vascular malformations via increased MEKK3-dependent KLF4 expression. *Circ Res*. 2019;124:1240-1252.
28. Zhu X, Bergles DE, Nishiyama A. NG2 Cells generate both oligodendrocytes and gray matter astrocytes. *Development*. 2008;135:145-157.
29. Hill RA, Tong L, Yuan P, Murikinati S, Gupta S, Grutzendler J. Regional blood flow in the normal and ischemic brain is controlled by arteriolar smooth muscle cell contractility and not by capillary pericytes. *Neuron*. 2015;87:95-110.
30. Whitehead KJ, Chan AC, Navankasattusas S, *et al*. The cerebral cavernous malformation signaling pathway promotes vascular integrity via rho GTPases. *Nat Med*. 2009;15:177-184.
31. Jenny Zhou H, Qin L, Zhang H, *et al*. Endothelial exocytosis of angiopoietin-2 resulting from CCM3 deficiency contributes to cerebral cavernous malformation. *Nat Med*. 2016;22:1033-1042.
32. Girard R, Fam MD, Zeineddine HA, *et al*. Vascular permeability and iron deposition biomarkers in longitudinal follow-up of cerebral cavernous malformations. *J Neurosurg*. 2017;127:102-110.
33. Madisen L, Zwingman TA, Sunkin SM, *et al*. A robust and high-throughput cre reporting and characterization system for the whole mouse brain. *Nat Neurosci*. 2010;13:133-140.
34. Chan-Ling T, Page MP, Gardiner T, Baxter L, Rosinova E, Hughes S. Desmin ensheathment ratio as an indicator of vessel stability: Evidence in normal development and in retinopathy of prematurity. *Am J Pathol*. 2004;165:1301-1313.
35. Armulik A, Genove G, Mae M, *et al*. Pericytes regulate the blood-brain barrier. *Nature*. 2010;468:557-561.
36. Daneman R, Zhou L, Kebede AA, Barres BA. Pericytes are required for blood-brain barrier integrity during embryogenesis. *Nature*. 2010;468:562-566.
37. Cuttler AS, LeClair RJ, Stohn JP, *et al*. Characterization of pdgfrb-cre transgenic mice reveals reduction of ROSA26 reporter activity in remodeling arteries. *Genesis*. 2011;49:673-680.
38. Mizushima N, Levine B, Cuervo AM, Klionsky DJ. Autophagy fights disease through cellular self-digestion. *Nature*. 2008;451:1069-1075.
39. Linares JF, Duran A, Reina-Campos M, *et al*. Amino acid activation of mTORC1 by a PB1-domain-driven kinase Complex cascade. *Cell Rep*. 2015;12:1339-1352.
40. Castillo SD, Tzouanacou E, Zaw-Thin M, *et al*. Somatic activating mutations in Pik3ca cause sporadic venous malformations in mice and humans. *Sci Transl Med*. 2016;8:332ra43.
41. Boscolo E, Limaye N, Huang L, *et al*. Rapamycin improves TIE2-mutated venous malformation in murine model and human subjects. *J Clin Invest*. 2015;125:3491-3504.
42. Fish JE, Flores Suarez CP, Boudreau E, *et al*. Somatic gain of KRAS function in the endothelium is sufficient to cause vascular malformations that require MEK but not PI3K signaling. *Circ Res*. 2020;127:727-743.
43. Park ES, Kim S, Huang S, *et al*. Selective endothelial hyperactivation of oncogenic KRAS induces brain arteriovenous malformations in mice. *Ann Neurol*. 2021;89:926-941.
44. Ren J, Jiang N, Bian L, *et al*. Natural history of spinal cord cavernous malformations: A Multicenter Cohort Study. *Neurosurgery*. 2022;90:390-398.
45. Stapleton CJ, Barker FG. 2nd. Cranial cavernous malformations: Natural history and treatment. *Stroke*. 2018;49:1029-1035.
46. Badhiwala JH, Farrokhyar F, Alhazzani W, *et al*. Surgical outcomes and natural history of intramedullary spinal cord cavernous malformations: a single-center series and meta-analysis of individual patient data: clinic article. *J Neurosurg Spine*. 2014;21:662-676.
47. Akers A, Al-Shahi Salman R, AA I, *et al*. Synopsis of guidelines for the clinical management of cerebral cavernous malformations: Consensus recommendations based on systematic literature review by the angioma alliance scientific advisory board clinical experts panel. *Neurosurgery*. 2017;80:665-680.
48. Snellings DA, Hong CC, Ren AA, *et al*. Cerebral cavernous malformation: From mechanism to therapy. *Circ Res*. 2021;129:195-215.
49. Huo R, Wang J, Sun YF, *et al*. Simplex cerebral cavernous malformations with MAP3K3 mutation have distinct clinical characteristics. *Front Neurol*. 2022;13:946324.